

# CALIBRATING SENSING DRIFT IN TOMOGRAPHIC INVERSION

Xiang Huang<sup>1</sup>, Stefan M. Wild<sup>1</sup>, Zichao (Wendy) Di<sup>1,2</sup>

<sup>1</sup>Mathematics and Computer Science Division, Argonne National Laboratory, Lemont, IL 60439, USA

<sup>2</sup>Advanced Photon Source, Argonne National Laboratory, Lemont, IL 60439, USA

## ABSTRACT

Scanning-probe x-ray tomography is useful for imaging nanoscale structures of a sample. The image resolution, which can reach down to 10 nm by the increased brightness and coherence of the x-ray optics, however, is highly susceptible to experimental error. Failure to address these errors can lead to a smeared image and, in the worst case, to misinterpretation of the imaged object's structure. In this work, we present a novel optimization-based approach to calibrate a common yet challenging source of experimental error, the drifts of the scanning positions, while simultaneously reconstructing the object. This approach utilizes the coupled and complementary information from different measurements to inform a coherent system between the measurements and the reconstruction. We illustrate the proposed approach on both synthetic and real tomography images and show its superior performance compared without explicit error calibration.

**Index Terms**—tomography, inverse problem, error calibration, compressive sensing

## 1. INTRODUCTION

X-ray tomography is an effective tool to reveal the internal structure of a 3D sample and plays an essential role in scientific areas from materials science to environmental science [1, 2]. It uses x-rays to generate many measurements from different angles of view in order to produce a cross-sectional image of the scanned object. In order to achieve high spatial resolution, x-ray tomography is often coupled with scanning probe microscopy (SPM), where a small x-ray beam is raster-scanned through the object. This technique is becoming popular in a growing number of applications [3, 4]. With recent advances in the development of x-ray optics, the image resolution provided by scanning probe x-ray tomography can reach down to 10 nm and below [5] but is drastically degraded by the error in the scanning positions.

Thermal drift, center of rotation drift, sample drift, vibrations, and other mechanical errors in the experimental equipment when undertaking experiments can lead to errors in the scanning positions. For example, Hüe et al. [6, 7] observed the error of the scanning positions of the same order as the expected spatial resolution over the course of an experiment. As illustrated in Fig. 1, the effect of scanning position drifts on the reconstruction quality can be crucial. Given a standard Shepp-Logan phantom as the object, the left panel shows the

tomographic data (namely, the sinogram) without any drift. The middle panel shows the sinogram with a maximum drift that is no more than the expected spatial resolution. The right panel shows the sinogram with a maximum drift of 5 times the expected spatial resolution. As we can see, the bigger the drift is, the more distorted and jittered the sinogram can be. Since these experimental errors are not fully avoidable, it is desirable to recover them numerically.

When the drifts of scanning positions are small compared with the beam width, one can address these errors by incorporating prior knowledge into the reconstruction using Bayesian frameworks [8–10]. The improvement in optical imaging hardware has been so great, however, that the generic approaches are not likely to be sufficient. In full-field tomography, efforts have focused on the most dominant error, the drifts of the center of rotations [11–13], through feature- or optimization-based strategies. In SPM, various approaches to explicitly address the scanning position errors have been reported in [14–18], which include simulated annealing, model-based drift correction, and cross-correlations of the shadow images. These approaches are model-specific and impractical, however, because of their complexity in the context of general tomographic reconstruction.

In this work, we explore the correlation and complementary information among the projections and propose an optimization-based reconstruction scheme to simultaneously calibrate the error of the scanning positions and reconstruct the object. We confine ourselves to the case where the error of the scanning positions is caused by the drifts of the scanning positions. More specifically, the scanning positions are assumed to be equally spaced with a fixed step size in the ideal case without drifts. However, the drifts can cause uneven spacing or, worse, swapping of the scanning positions. Our proposed approach preserves the flexibility of incorporating prior knowledge, while enabling an easier automation than the existing approaches. Furthermore, it can be more robust in the context of poor and limited data.

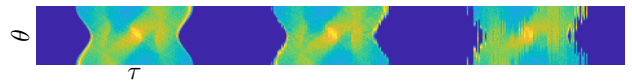


**Fig. 1:** Comparison of sinograms showing effects of scanning position drift. Left: drift-free sinogram; middle: sinogram with a maximum drift of 1 expected spatial resolution; right: sinogram with a maximum drift of 5 times the expected spatial resolution.

In Sec. 2, we describe our mathematical formulation of the error of the scanning positions during the course of the experiment and show how to embed these models in the reconstruction scheme. In Sec. 3, we introduce the reconstruction algorithm along with our method for drift calibration. In Sec. 4, we present numerical simulations and compare the proposed approach with the existing approach using both synthetic and real images. In Sec. 5, we summarize the proposed method and discuss a few future directions. For brevity, we focus on 2D reconstruction; extension to the 3D case with a parallel beam is straightforward.

## 2. PROBLEM FORMULATION

In x-ray tomography, the Radon transform [19] provides the forward model from object to measurement, where the discrete case is described below. Given a 2D object, we discretize it as  $N \times N$  pixels whose indices are vectorized with an array  $\mathcal{V}$ . We denote by  $\mathbf{w}_v$  the pixel intensity at  $v \in \mathcal{V}$ , that is, the value of the object property we intend to recover such as attenuation coefficient for x-ray transmission and refractive index in ultrasound tomography. We denote by  $\mathbf{w} = \{\mathbf{w}_v : v \in \mathcal{V}\} \in \mathbb{R}^{N^2 \times 1}$  the discretized object. In the ideal case without drifts of the scanning positions, the object is scanned with  $N_\theta$  rotations denoted by  $\theta \in \{1, \dots, N_\theta\}$ , and each rotation is raster scanned with  $N_\tau$  fixed step sizes denoted by  $\tau \in \{1, \dots, N_\tau\}$ . The whole scan results in a 2D sinogram,  $\mathbf{S} \in \mathbb{R}^{N_\theta \times N_\tau}$ . Let  $L_v^{\theta, \tau}$  be the intersection length of the beam  $(\theta, \tau)$  with the pixel  $v \in \mathcal{V}$ . Then the tensor  $\mathbf{L} = [L_v^{\theta, \tau}] \in \mathbb{R}^{N_\theta N_\tau \times N^2}$  defines the forward map from the object to the sinogram:  $\mathbf{s} = \mathbf{L}\mathbf{w}$ , where  $\mathbf{s} \in \mathbb{R}^{N_\theta N_\tau \times 1}$  is the lexicographical (column-first) reordered vector of  $\mathbf{S}$ .

Given the forward model  $\mathbf{L}$  and the measurement  $\mathbf{s}$ , we can reconstruct the object  $\mathbf{w}$  by solving the following optimization problem:

$$\min_{\mathbf{w} \geq 0} \frac{1}{2} \|\mathbf{L}\mathbf{w} - \mathbf{s}\|^2 + \lambda \Phi(\mathbf{w}), \quad (2.1)$$

where  $\Phi(\mathbf{w})$  is a regularizer (e.g., total variation (TV) [20]) to incorporate prior knowledge and  $\lambda \geq 0$  is a scalar balancing the data misfit (e.g., noise, model error) and regularizer.

In the presence of the drifts of the scanning positions, the true forward model denoted by  $\bar{\mathbf{L}}$  will be different from the theoretical model  $\mathbf{L}$  because of the different scanning positions. Fig. 2 illustrates the geometric sketch of the experiment with the drifts of the scanning positions. Beam  $\tau$  without drift (which is referred as the assumed scanning position) is shown as the green line, given the constant scanning step  $\Delta$ . Correspondingly, its drifted position with drift  $\Delta_\tau$  is shown as the purple line. In practice, one can expect a manual calibration before each rotation during the course of the experiment. Then, for simplicity, we can reasonably assume that the drifts of the scanning positions are the same after any rotation, so that drift  $\Delta_\tau$  depends only on  $\tau$  (and not on  $\theta$ ).

We now study how drifts affect the forward model  $\mathbf{L}$ . We

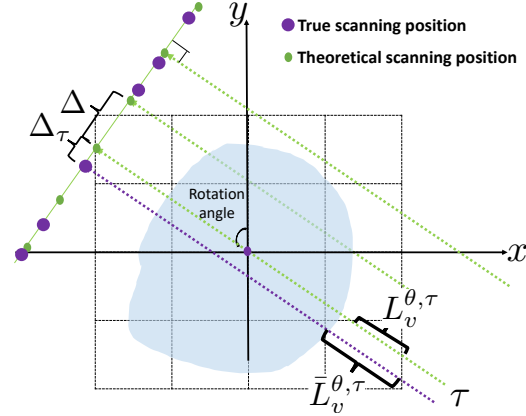


Fig. 2: Geometric sketch of the drifts of the scanning positions in tomography.

first consider a simple case where any drift of the scanning positions is an integer multiple of the theoretical spacing  $\Delta$  as in Prop. 2.1.

**Proposition 2.1** (Integer drifts). *If  $\forall \tau \in \{1, \dots, N_\tau\}$ ,  $\Delta_\tau$  is an integer multiple of  $\Delta$ , then  $\bar{\mathbf{L}}\mathbf{w} \subseteq \mathbf{L}\mathbf{w}$ <sup>1</sup>. Furthermore, there exists a binary row selection matrix  $\mathbf{P} \in \mathbb{R}^{N_\theta N_\tau \times N_\theta N_\tau}$*

*such that  $\bar{\mathbf{L}} = \mathbf{P}\mathbf{L}$ , where  $\forall(\theta, \tau)$ ,  $\sum_{j=1}^{N_\theta N_\tau} \mathbf{P}_{(\tau-1)N_\theta + \theta, j} \leq 1$ , and*

$$\mathbf{P}_{(\tau-1)N_\theta + \theta, (\tau'-1)N_\theta + \theta} = \begin{cases} 1 & \forall \theta, \text{ if the assumed scanning position of beam } \tau \\ & \text{is drifted to the position of beam } \tau', \\ 0 & \text{otherwise.} \end{cases} \quad (2.2)$$

Next we consider the more challenging and practical case that drifts  $\Delta_\tau$  are not integer multiples of  $\Delta$ . In this case  $\bar{\mathbf{L}}\mathbf{w}$  is not necessarily a subset of the drift-free  $\mathbf{L}\mathbf{w}$ ; hence  $\bar{\mathbf{L}}$  cannot be obtained directly from row selection of  $\mathbf{L}$ .

However, assuming that the 1D integration of a 2D object along any angular direction (i.e., the 2D sinogram along the  $\tau$  direction) is smooth<sup>2</sup>, we can approximate  $\bar{\mathbf{L}} \approx \mathbf{P}\mathbf{L}$ , where  $\mathbf{P}$  selects and interpolates the rows of  $\mathbf{L}$ . For example, linear interpolation uses two adjacent beamlets to interpolate between; hence each row of  $\mathbf{P}$  has only two adjacent nonzero elements,

$$\mathbf{P}_{(\tau-1)N_\theta + \theta, (\tau'-1)N_\theta + \theta} = \begin{cases} \alpha_\tau & \text{if } \tau' + 1 = \lfloor \frac{\Delta_\tau}{\Delta} \rfloor, \\ 1 - \alpha_\tau & \text{if } \tau' = \lfloor \frac{\Delta_\tau}{\Delta} \rfloor, \\ 0 & \text{otherwise.} \end{cases} \quad (2.3)$$

where  $\alpha_\tau = \frac{\Delta_\tau}{\Delta} - \lfloor \frac{\Delta_\tau}{\Delta} \rfloor \in [0, 1)$  denotes the fractional part of the drift  $\tau$ . We denote the corresponding integer part by

<sup>1</sup>Here  $\mathbf{a} \subseteq \mathbf{b}$  for two vectors means that components of the vector  $\mathbf{a}$  are a subset of components of the vector  $\mathbf{b}$ .

<sup>2</sup>This is weaker than assuming that the 2D object itself is smooth due to the integration.

$$\pi_\tau = \lfloor \frac{\Delta_\tau}{\Delta} \rfloor.$$

Similarly, a quadratic or higher-order interpolation can be carried out but with three or more nonzero elements per row in  $\mathbf{P}$ . For simplicity, we focus on linear interpolation in this work.

We now formulate the reconstruction with drift calibration as the following optimization problem:

$$\min_{\mathbf{w} \geq 0, \mathbf{P}} \frac{1}{2} \|\mathbf{P}\mathbf{L}\mathbf{w} - \mathbf{s}\|^2 + \lambda \Phi(\mathbf{w}). \quad (2.4)$$

### 3. OPTIMIZATION-BASED RECONSTRUCTION ALGORITHM

Our goal is to estimate the unknown drift matrix  $\mathbf{P}$  and object  $\mathbf{w}$  from the measurement  $\mathbf{s}$  in (2.4). In Algorithm 1, we propose to iteratively solve problem (2.4) by alternating between using the current estimate  $\mathbf{P}$  to reconstruct the object  $\mathbf{w}$  and using the current reconstruction to update  $\mathbf{P}$ . We explore the TwIST solver [21] to solve the intermediate reconstruction step 5. At each iteration of TwIST, we enforce the nonnegative constraint by projecting the negative components of  $\mathbf{w}$  to 0, which yields faster convergence and better reconstruction. Algorithm 2 describes how we compute the  $N_\tau$  unknown drifts by matching the measurement  $\mathbf{s}$  with the  $\mathbf{L}\mathbf{w}$  based on the current reconstruction  $\mathbf{w}$ . To obtain fast convergence for large drifts, we use a large regularization parameter value,  $\eta\lambda$ , in the beginning and gradually reduce it to  $\lambda$ . Notice that alternatively, once the recovered drifts  $\Delta_\tau$  are stable after  $k$  iterations, we can explicitly generate the stabilized  $\bar{\mathbf{L}}$  from the drifts, rather than by using interpolation, to carry out our final reconstruction.

---

#### Algorithm 1 Tomographic Reconstruction with Drift Calibration

---

- 1: Input:  $\mathbf{s}, \mathbf{L}, \lambda$ , maximum number of iterations  $k_{\max}$  (e.g., 10), and scalar  $\eta$  (e.g., 100).
- 2: Initialize  $\mathbf{L}^0 = \mathbf{L}$
- 3: **for**  $k = 1, 2, \dots, k_{\max}$  **do**
- 4:    $\lambda_k \leftarrow \lambda \left( \eta - (\eta - 1) \frac{k-1}{k_{\max}-1} \right)$ .
- 5:   Use TwIST to solve:

$$\mathbf{w}^k = \arg \min_{\mathbf{w} \geq 0} \frac{1}{2} \|\mathbf{L}^{k-1} \mathbf{w} - \mathbf{s}\|^2 + \lambda_k \Phi(\mathbf{w}) \quad (3.5)$$

- 6:   Use Algorithm 2 to solve:

$$\mathbf{P}^k = \arg \min_{\mathbf{P} \in \mathcal{P}} \frac{1}{2} \|\mathbf{P}\mathbf{L}\mathbf{w}^k - \mathbf{s}\|^2 + \lambda_k \Phi(\mathbf{w}^k),$$

where  $\mathcal{P}$  is the set of allowable  $\mathbf{P}$  based on prior knowledge such as maximum possible drift.

- 7:  $\mathbf{L}^k \leftarrow \mathbf{P}^k \mathbf{L}$
  - 8: Output:  $\mathbf{w}^k, \mathbf{P}^k, \mathbf{L}^k$
- 

To compute the current drift  $\mathbf{P}^k$  in Algorithm 1 step 6, we

first reshape vectors  $\mathbf{L}\mathbf{w}^k$  and  $\mathbf{P}\mathbf{L}\mathbf{w}^k$  to 2D matrices  $\mathbf{S}^*$  and  $\bar{\mathbf{S}}$  of size  $\mathbb{R}^{N_\theta \times N_\tau}$ , respectively. We then rewrite the objective function  $\|\mathbf{P}\mathbf{L}\mathbf{w}^k - \mathbf{s}\|^2$  as  $\|\bar{\mathbf{S}} - \mathbf{S}\|_F^2$ , where  $\|\cdot\|_F$  denotes the Frobenius norm. Here we dropped the regularization term  $\lambda_k \Phi(\mathbf{w}^k)$  because it is independent of  $\mathbf{P}$ . For linear interpolation,

$$\bar{\mathbf{S}}_{\cdot\tau} = (1 - \alpha_\tau) \mathbf{S}^*_{\cdot\tau + \pi_\tau} + \alpha_\tau \mathbf{S}^*_{\cdot\tau + \pi_\tau + 1}, \quad (3.6)$$

where  $\cdot\tau$  denotes the  $\tau$ th column of a matrix. In practice, we restrict the drifts to fall in  $[-\Delta_{\max}, \Delta_{\max}]$ ; hence  $\pi_\tau \in [-\pi_{\max}, \pi_{\max}]$ , where  $\pi_{\max} = \lceil \frac{\Delta_{\max}}{\Delta} \rceil$ . The main complexity of Algorithm 2 is in step 3 for solving problem (3.7). More specifically, we compute each drift  $\Delta_\tau$  independently by swapping  $\pi_\tau$  from  $-\pi_{\max}$  to  $\pi_{\max}$ . Notice that the scalar  $\alpha_\tau$  can be directly calculated with a given  $\pi_\tau$  by setting its corresponding derivative of problem (3.7) to 0. Therefore, the total cost of solving (3.7), given  $N_\theta$  angles and  $N_\tau$  beamlets, is  $O(N_\theta N_\tau \pi_{\max})$ .

---

#### Algorithm 2 Calibration of Drift Error

---

- 1: Input:  $\mathbf{s}, \mathbf{L}, \mathbf{w}^k$
- 2: Construct 2D matrices  $\mathbf{S}$  and  $\mathbf{S}^*$  from  $\mathbf{s}$  and  $\mathbf{L}\mathbf{w}^k$
- 3: For  $\tau = 1, \dots, N_\tau$ , solve

$$\min_{\substack{\pi_\tau \in [-\pi_{\max}, \pi_{\max}] \\ \alpha_\tau \in [0, 1]}} \sum_{\tau=1}^{N_\tau} \|\mathbf{S}_{\cdot\tau} - (1 - \alpha_\tau) \mathbf{S}^*_{\cdot\tau + \pi_\tau} - \alpha_\tau \mathbf{S}^*_{\cdot\tau + \pi_\tau + 1}\|^2 \quad (3.7)$$

- 4: Compute  $\Delta_\tau = \pi_\tau + \alpha_\tau$ ; construct  $\mathbf{P}$  using Eq. (2.3)
  - 5: Output:  $\{\Delta_\tau, \tau = 1, \dots, N_\tau\}, \mathbf{P}$
- 

## 4. EXPERIMENTAL RESULTS

To validate the efficacy of our proposed method, we compare its performance with the regularized baseline reconstruction that directly solves problem (2.1). We confine ourselves to the TV regularization as one of the most popular choices in the community of tomographic reconstruction [22, 23]. We choose two images as the testing objects: the standard synthetic Shepp-Logan phantom and the real MRI brain image, which are shown in Fig. 3 as the ground truth. We map the original grayscale test images with the colormap in Fig. 3 to reveal more details. For the experimental configuration, we fix the image resolution  $N = 100$ , the number of rotations  $N_\theta = 45$ , and the number of beamlets  $N_\tau = 152$ , which means  $N_\tau \Delta \geq \sqrt{2}N\Delta + 10\Delta$ , to guarantee the full coverage of the object in at least 5 scans outside of the object of interest on both sides.

We perform tests for different levels of drifts separately; namely,  $\max \Delta_\tau \in \{\Delta, 2\Delta, 3\Delta, 5\Delta\}$ . For each case, to further test the robustness of our proposed method, we add two levels of Gaussian noise to the sinogram (simulated with the assigned drifts) with standard deviation  $\sigma$  (relative to the maximum intensity of its corresponding noise-free sinogram) as

**Table 1:** Performance comparison of our method with the baseline method for four drift levels and three noise levels. Blue row: PSNR (dB); gray row: SSIM.

| Max Drift          | 1      |        |        | 2      |        |        | 3      |        |        | 5      |        |        |
|--------------------|--------|--------|--------|--------|--------|--------|--------|--------|--------|--------|--------|--------|
| Noise              | 0      | 0.01   | 0.02   | 0      | 0.01   | 0.02   | 0      | 0.01   | 0.02   | 0      | 0.01   | 0.02   |
| Brain (proposed)   | 27.17  | 24.28  | 20.43  | 25.72  | 23.55  | 20.45  | 25.62  | 23.34  | 19.73  | 23.50  | 21.82  | 19.24  |
|                    | 0.8332 | 0.6052 | 0.4193 | 0.7826 | 0.5785 | 0.4052 | 0.7702 | 0.5677 | 0.3764 | 0.6824 | 0.5040 | 0.3374 |
| Brain (baseline)   | 22.06  | 21.27  | 19.09  | 17.22  | 17.03  | 16.06  | 14.58  | 14.43  | 13.78  | 11.83  | 11.76  | 11.45  |
|                    | 0.5291 | 0.4646 | 0.3515 | 0.2314 | 0.2174 | 0.1772 | 0.1056 | 0.1008 | 0.0852 | 0.0434 | 0.0427 | 0.0416 |
| Phantom (proposed) | 21.69  | 20.96  | 19.81  | 20.65  | 19.93  | 19.41  | 18.40  | 18.00  | 17.23  | 16.75  | 16.47  | 15.81  |
|                    | 0.7236 | 0.6396 | 0.5447 | 0.7004 | 0.6237 | 0.5364 | 0.6253 | 0.5597 | 0.4619 | 0.5722 | 0.5101 | 0.4237 |
| Phantom (baseline) | 14.57  | 14.47  | 14.21  | 12.38  | 11.83  | 11.82  | 10.88  | 10.89  | 11.08  | 9.97   | 9.98   | 9.96   |
|                    | 0.4699 | 0.4472 | 0.4113 | 0.3091 | 0.2856 | 0.2686 | 0.2422 | 0.2299 | 0.2188 | 0.2137 | 0.2062 | 0.1958 |

0.01 and 0.02, respectively. We adopt two error metrics, the peak signal-to-noise ratio (PSNR) and the structural similarity index (SSIM) [24], to quantify the reconstruction quality. All experiments use  $\lambda = 1.3 \times 10^{-5}$ , which is the weight that yields the best PSNR for the baseline algorithm for the brain sample with maximum drift  $\Delta$ .

Table 1 shows the full comparison results. Clearly, our proposed method stably outperforms the baseline method in terms of both reconstruction quality metrics. On average, our method results in higher PSNR (by 6.97 dB) and SSIM (by 0.3289) than the baseline method does, respectively.

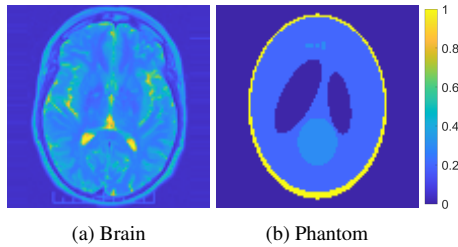


**Fig. 3:** Test images and colormap.

We also qualitatively compare the results of our method with the baseline method in Fig. 4. Because of space limits, we include only a few examples here. We observe that our method produces results much closer to the groundtruth object and significantly fewer visual artifacts compared with the baseline method.

## 5. DISCUSSION AND CONCLUSION

In this work, we address a pervasive source of experimental error, the drifts of the scanning positions, during the scanning-probe x-ray tomography by means of a numerical optimization approach. We propose a forward model to describe such error, and we develop an iterative optimization algorithm to calibrate the drifts while reconstructing the object following an alternating fashion. The numerical results suggest that our

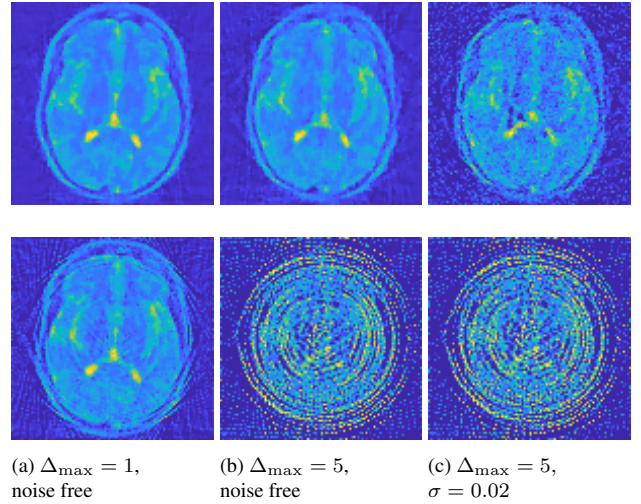


**Fig. 4:** Top row: proposed method with drift calibration; bottom row: baseline reconstruction.

method outperforms the current practice by explicitly calibrating the amount of drifts and that the method recovers the tested objects to a satisfying degree. Our method can be naturally extended to 3D reconstruction with a parallel x-ray beam. One aspect we can further explore is to incorporate prior knowledge about the drifts (e.g., dynamics, pattern) to speed the calibration performance. In order to further stabilize the performance of our optimization-based approach, rigorous convergence analysis should be carried out.

## Acknowledgments

This material was based upon work supported by the U.S. Department of Energy, Office of Science, Office of Advanced Scientific Computing Research's applied mathematics program under contract DE-AC02-06CH11357.

## 6. REFERENCES

- [1] J. Baruchel, J.-Y. Buffiere, and E. Maire, *X-Ray Tomography in Material Science*. Hermes Science Publications, 2000.
- [2] M. J. Paulus, S. S. Gleason, S. J. Kennel, P. R. Hunsicker, and D. K. Johnson, "High resolution x-ray computed tomography: an emerging tool for small animal cancer research," *Neoplasia*, vol. 2, no. 1-2, pp. 62–70, 2000.
- [3] M. D. de Jonge and S. Vogt, "Hard x-ray fluorescence tomography—an emerging tool for structural visualization," *Current Opinion in Structural Biology*, vol. 20, no. 5, pp. 606–614, 2010.
- [4] M. Dierolf, A. Menzel, P. Thibault, P. Schneider, C. M. Kewish, R. Wepf, O. Bunk, and F. Pfeiffer, "Ptychographic x-ray computed tomography at the nanoscale," *Nature*, vol. 467, no. 7314, p. 436, 2010.
- [5] H. Yan, N. Bouet, J. Zhou, X. Huang, E. Nazaretski, W. Xu, A. P. Cocco, W. K. Chiu, K. S. Brinkman, and Y. S. Chu, "Multimodal hard x-ray imaging with resolution approaching 10 nm for studies in material science," *Nano Futures*, vol. 2, no. 1, p. 011001, 2018.
- [6] F. H  , J. Rodenburg, A. Maiden, and P. Midgley, "Extended ptychography in the transmission electron microscope: Possibilities and limitations," *Ultramicroscopy*, vol. 111, no. 8, pp. 1117–1123, 2011.
- [7] F. H  , J. Rodenburg, A. Maiden, F. Sweeney, and P. Midgley, "Wave-front phase retrieval in transmission electron microscopy via ptychography," *Physical Review B*, vol. 82, no. 12, p. 121415, 2010.
- [8] W. van Aarle, K. J. Batenburg, G. Van Gompel, E. Van de Casteele, and J. Sijbers, "Super-resolution for computed tomography based on discrete tomography," *IEEE Transactions on Image Processing*, vol. 23, no. 3, pp. 1181–1193, 2014.
- [9] P. Charbonnier, L. Blanc-F  raud, G. Aubert, and M. Barlaud, "Deterministic edge-preserving regularization in computed imaging," *IEEE Transactions on Image Processing*, vol. 6, no. 2, pp. 298–311, 1997.
- [10] K. Sauer, J. Sachs, and C. Klifa, "Bayesian estimation of 3-D objects from few radiographs," *IEEE Transactions on Nuclear Science*, vol. 41, no. 5, pp. 1780–1790, 1994.
- [11] A. Austin, Z. W. Di, S. Leyffer, and S. M. Wild, "Simultaneous sensing error recovery and tomographic inversion using an optimization-based approach," *SIAM Journal on Scientific Computing*, 2019, to appear.
- [12] M. Cao, A. Takaoka, H.-B. Zhang, and R. Nishi, "An automatic method of detecting and tracking fiducial markers for alignment in electron tomography," *Journal of Electron Microscopy*, vol. 60, no. 1, pp. 39–46, 2010.
- [13] D. G  rsoy, Y. P. Hong, K. He, K. Hujsak, S. Yoo, S. Chen, Y. Li, M. Ge, L. M. Miller, Y. S. Chu *et al.*, "Rapid alignment of nanotomography data using joint iterative reconstruction and reprojection," *Scientific Reports*, vol. 7, no. 1, p. 11818, 2017.
- [14] M. Beckers, T. Senkbeil, T. Gorniak, K. Giewekemeyer, T. Salditt, and A. Rosenhahn, "Drift correction in ptychographic diffractive imaging," *Ultramicroscopy*, vol. 126, pp. 44–47, 2013.
- [15] A. Tripathi, I. McNulty, and O. G. Shpyrko, "Ptychographic overlap constraint errors and the limits of their numerical recovery using conjugate gradient descent methods," *Optics Express*, vol. 22, no. 2, pp. 1452–1466, 2014.
- [16] F. Zhang, I. Peterson, J. Vila-Comamala, A. Diaz, F. Berenguer, R. Bean, B. Chen, A. Menzel, I. K. Robinson, and J. M. Rodenburg, "Translation position determination in ptychographic coherent diffraction imaging," *Optics Express*, vol. 21, no. 11, pp. 13 592–13 606, 2013.
- [17] A. Hurst, T. Edo, T. Walther, F. Sweeney, and J. Rodenburg, "Probe position recovery for ptychographical imaging," in *Journal of Physics: Conference Series*, vol. 241, no. 1. IOP Publishing, 2010, p. 012004.
- [18] X. Sang and J. M. LeBeau, "Revolving scanning transmission electron microscopy: Correcting sample drift distortion without prior knowledge," *Ultramicroscopy*, vol. 138, pp. 28–35, 2014.
- [19] A. C. Kak and M. Slaney, *Principles of Computerized Tomographic Imaging*. IEEE Press, 1988.
- [20] H. W. Engl, M. Hanke, and A. Neubauer, *Regularization of Inverse Problems*. Springer Science & Business Media, 1996, vol. 375.
- [21] J. M. Bioucas-Dias and M. A. Figueiredo, "A new TwIST: two-step iterative shrinkage/thresholding algorithms for image restoration," *IEEE Transactions on Image Processing*, vol. 16, no. 12, pp. 2992–3004, 2007.
- [22] W. Li-yan and W. Zhi-hui, "Fast gradient-based algorithm for total variation regularized tomography reconstruction," in *Image and Signal Processing (CISP), 2011 4th International Congress on*, vol. 3. IEEE, 2011, pp. 1572–1576.
- [23] F. Mahmood, N. Shahid, U. Skoglund, and P. Vandebergheynst, "Adaptive graph-based total variation for tomographic reconstructions," *IEEE Signal Processing Letters*, vol. 25, no. 5, pp. 700–704, 2018.
- [24] A. Hore and D. Ziou, "Image quality metrics: PSNR vs. SSIM," in *20th International Conference on Pattern Recognition (ICPR)*. IEEE, 2010, pp. 2366–2369.